Monthly Notices
of the
ROYAL ASTRONOMICAL SOCIETY

MNRAS **483,** 873–886 (2019)
Advance Access publication 2018 November 22

doi:10.1093/mnras/sty3132

# The solar wind in time – II. 3D stellar wind structure and radio emission

D. Ó Fionnagáin [1]★ A. A. Vidotto [1] P. Petit,[2,3] C. P. Folsom,[2,3] S. V. Jeffers,[4] S. C. Marsden,[5] J. Morin,[6] J.-D. do Nascimento, Jr[7,8] and the BCool Collaboration

[1] *School of Physics, Trinity College Dublin, College Green, Dublin 2, Ireland*
[2] *Institut de Recherche en Astrophysique et Planétologie, Université de Toulouse, UPS-OMP, F-31400 Toulouse, France*
[3] *IRAP, Université de Toulouse, CNRS, UPS, CNES, F-31400 Toulouse, France*
[4] *Institut für Astrophysik, Universität Göttingen, Friedrich-Hund-Platz 1, D-37077 Göttingen, Germany*
[5] *Centre for Astrophysics, University of Southern Queensland, Toowoomba, QLD 4350, Australia*
[6] *Laboratoire Univers et Particules de Montpellier, Université de Montpellier, CNRS, F-34095 Montpellier, France*
[7] *Dep. de Física, Universidade Federal do Rio Grande do Norte, CEP: 59072-970 Natal, RN, Brazil*
[8] *Harvard-Smithsonian Center for Astrophysics, Cambridge, MA 02138, USA*

Accepted 2018 November 12. Received 2018 November 2; in original form 2018 September 13

## ABSTRACT

In this work, we simulate the evolution of the solar wind along its main-sequence lifetime and compute its thermal radio emission. To study the evolution of the solar wind, we use a sample of solar mass stars at different ages. All these stars have observationally reconstructed magnetic maps, which are incorporated in our 3D magnetohydrodynamic simulations of their winds. We show that angular-momentum loss and mass-loss rates decrease steadily on evolutionary time-scales, although they can vary in a magnetic cycle time-scale. Stellar winds are known to emit radiation in the form of thermal bremsstrahlung in the radio spectrum. To calculate the expected radio fluxes from these winds, we solve the radiative transfer equation numerically from first principles. We compute continuum spectra across the frequency range 100 MHz to 100 GHz and find maximum radio flux densities ranging from 0.05 to 2.2 μJy. At a frequency of 1 GHz and a normalized distance of $d = 10$ pc, the radio flux density follows $0.24\ (\Omega/\Omega_\odot)^{0.9}\ (d/[10\mathrm{pc}])^{-2}$ μJy, where Ω is the rotation rate. This means that the best candidates for stellar wind observations in the radio regime are faster rotators within distances of 10 pc, such as $\kappa^1$ Ceti (0.73 μJy) and $\chi^1$ Ori (2.2 μJy). These flux predictions provide a guide to observing solar-type stars across the frequency range 0.1–100 GHz in the future using the next generation of radio telescopes, such as ngVLA and Square Kilometre Array.

**Key words:** stars: solar-type – stars: winds, outflows – radio continuum: stars .

## 1 INTRODUCTION

Solar analogues are essential to our understanding of how our own Sun has evolved through its past and how it will evolve into the future. The rotational evolution of stars has a significant effect on the activity (Wright et al. 2011; Vidotto et al. 2014b), as rotation has been linked to activity markers such as coronal X-ray emission (Telleschi et al. 2005; Wright et al. 2011), chromospheric activity (e.g. Ca II, H $\alpha$) (Lorenzo-Oliveira et al. 2018) and flaring rates (Maehara et al. 2017). The stellar dynamo is regulated by rotation and convection, which in turn generates the magnetic field causing stellar activity (Brun & Browning 2017). By virtue of this relationship between rotation and activity, the evolution of orbiting planets is directly affected, e.g. by high-energy stellar radiation incident on their atmospheres (Owen & Mohanty 2016; Ribas et al. 2016). Stellar rotation has been shown to decrease with age (Skumanich 1972) following $\Omega \propto t^{1/2}$ for stars older than ∼700 Myr (Gallet & Bouvier 2013). More recently, however, some deviation from this standardized age–rotation relationship has been observed at older ages (Van Saders et al. 2016), with some processes proposed to explain this behaviour (Metcalfe, Egeland & van Saders 2016; Beck et al. 2017; Booth et al. 2017; Ó Fionnagáin & Vidotto 2018).

The mechanism by which stars spin-down while traversing the main sequence is through angular momentum loss by their magnetized winds (e.g. Weber et al. 1967; Vidotto et al. 2014a; See et al. 2017b). Therefore, this indicates that the surface magnetic field of the star also evolves with time, as demonstrated with magnetic field observations analysed using the Zeeman–Doppler Imaging (ZDI) technique (Vidotto et al. 2014b; Folsom et al. 2016, 2018). ZDI is a method that allows for the reconstruction of the large-scale magnetic field of the stellar surface from a set of high-resolution

★ E-mail: ofionnad@tcd.ie

spectropolarimetric data (Semel 1989; Brown et al. 1991; Donati et al. 1997), although it is insensitive to small-scale fields (Lang et al. 2014; Lehmann et al. 2018). See et al. (2017a,b) determined, from 66 ZDI-observed stars, that the magnetic geometry as well as angular momentum and mass-loss is correlated to Rossby number.[1] Other works have demonstrated that there is a link between all of stellar activity, magnetic strength and geometry, angular momentum loss, and stellar winds (Matt et al. 2012; Nicholson et al. 2016; Pantolmos & Matt 2017; Finley, Matt & See 2018).

Stellar angular momentum-loss depends upon how much mass is lost by their winds (Weber et al. 1967). Due to the tenuous nature of low-mass stellar winds, a direct measurement of their winds is difficult (e.g. Wood et al. 2005), but would prove extremely useful in the constraining of mass-loss rates and other global wind parameters. In this regard, the observations of radio emission from the winds of low-mass stars could provide meaningful constraints on wind density and mass-loss rate (Lim & White 1996; Güdel 2002; Villadsen et al. 2014; Fichtinger et al. 2017; Vidotto & Donati 2017). The wind is expected to have continuum emission in radio through the mechanism of thermal free–free emission (Panagia & Felli 1975; Wright, Barlow & Michael 1975). This emission is expected to be stronger for stars with denser winds and is also dependent on the density ($n$) gradient in the wind with radial distance, $R$: $n \propto R^{-a}$. The value of $a$ is indirectly related to other stellar parameters such as the specific gravity, magnetic field, and rotation. When $a = 2$ this represents when the wind has reached terminal radial velocity, however, this is unrealistic in regions closer to the star where the wind is accelerating. Therefore, we expect stellar winds to exhibit gradients much steeper than when $a = 2$. We discuss this further in Section 4.

With this idea in mind, Güdel, Guinan & Skinner (1998) and Gaidos, Güdel & Blake (2000) observed various solar analogues. They could place upper limits on the radio fluxes from these objects, and so indirectly infer upper mass-loss rate constraints. All non-degenerate stars emit some form of radio emission from their atmospheres (Güdel 2002). Although different radio emission mechanisms dominate at different layers in their atmosphere and wind (Güdel 2002). For example, detecting coronal radio flares at a given frequency implies the surrounding wind is optically thin at those frequencies, allowing for placement of upper mass-loss limits. In addition, Güdel (2007) noted that thermal emission should dominate at radio frequencies as long as no flares occur while observing. The three dominant thermal emission mechanisms the author described are bremsstrahlung from the chromosphere, cyclotron emission above active regions, and coronal bremsstrahlung from hot coronal loops. These emission mechanisms must be addressed when attempting to detect the winds of solar-type stars at radio frequencies.

Observing these winds can become difficult as the fluxes expected from these sources is at the μJy level (see upper limits placed by Gaidos et al. 2000; Villadsen et al. 2014; Fichtinger et al. 2017), and can be drowned out by chromospheric and coronal emission as described in the previous paragraph. Villadsen et al. (2014) observed three low-mass stars, with positive detections for all three stars in the Ku band (centred at 34.5 GHz) of the VLA, and non-detections at lower frequencies. They suggested that the detected emissions originate in the chromosphere of these stars, with some contributions from other sources of radio emission. If emanating from the chromosphere, these detections do not aid in constraining the wind. Fichtinger et al. (2017) more recently observed four solar-type stars with the VLA at radio frequencies, and provided upper limits to the mass-loss rates for each, ranging from $3 \times 10^{-12}$ to $7 \times 10^{-10}\,\mathrm{M}_{\odot}$ $\mathrm{yr}^{-1}$, depending on how collimated the winds are. Bower et al. (2016) observed radio emission from the young star V830 Tau, with which Vidotto & Donati (2017) were able to propose mass-loss rate constraints between $3 \times 10^{-10}$ and $3 \times 10^{-12}\,\mathrm{M}_{\odot}$ $\mathrm{yr}^{-1}$. Transient coronal mass ejections should also be observable, which would cause more issues in detecting the ambient stellar wind, but these events are expected to be relatively short and could also help in constraining transient mass-loss from these stars (Crosley et al. 2016).

To aid in the radio detection and interpretation of the winds of solar-type stars, we here quantify the detectability of the winds of six solar-like stars of different ages within the radio regime from 100 MHz to 100 GHz. We aim to study the effects ageing stellar winds have on different solar analogues along the main sequence, allowing us to constrain global parameters and quantify the local wind environment.

To do this, we conduct 3D magnetohydrodynamical simulations of winds of solar-type stars, investigating the main-sequence solar wind evolution in terms of angular-momentum loss rates ($\dot{J}$), mass-loss rates ($\dot{M}$), and wind structure. We then use the results of our simulations to quantify the detectability of the radio emission from the solar wind in time, that can help guiding and planning of future observations of solar-like winds. We present the sample of stars simulated and analysed in Section 2. Discussed in Section 3 is the stellar wind modelling and simulation results. Our models predict the evolution of $\dot{J}$, $\dot{M}$, and $\Phi_{\mathrm{open}}$ of the solar wind through time, while also constraining the planetary environment surrounding the host stars. In Section 4 we demonstrate how we calculate radio emission for each star and the resulting emissions and flux densities expected. Section 5 we conclude on the results presented in this work.

## 2 STELLAR SAMPLE

Our sample of solar-like stars was selected so as to closely resemble to Sun in both mass and radius. They cover a range of rotation rates (from 4.8 to 27 d or 1 to 5.6 $\Omega_{\odot}$) with ZDI reconstructed by Petit et al. (2008), do Nascimento, Jr. et al. (2016), and Petit et al. (in preparation) as part of the BCool collaboration. Gallet & Bouvier (2013, 2015) depict different age–rotation evolutionary tracks for a 1 $\mathrm{M}_{\odot}$ star, which converge at 800 Myr to the Skumanich law (Skumanich 1972). $\chi^1$ Ori follows the fast rotator track, while the rest of our stars exist beyond the convergence point. We note that HD 190771 and HD 76151 exhibit faster rotation than the Skumanich law, which could be due to uncertainties in their ages. The stars in our sample are listed below, see also Table 1 for stellar parameters, and Fig. 1 for observed ZDI maps.

**$\chi^1$ Orion** This star is both the youngest star and the fastest rotator we have simulated, with a rotation period of 4.8 d and an age of 0.5 Gyr (Vidotto et al. 2014b). This fast rotation should indicate a more active star than the slower rotators, which we see confirmed in the high-magnetic-field strengths. The large-scale magnetic geometry reconstructed with ZDI for this star displays a complex structure (Fig. 1), showing very un-dipolar like structure (Petit et al., in preparation). Note that the ZDI observations here include 10 spherical

[1]Rossby number (Ro) is defined as the ratio between stellar rotation and convective turnover time (Noyes et al. 1984).

**Table 1.** Stellar parameters of our sample are shown on the left (mass, radius, rotation period, age, and distance) and specifics of the simulations are shown on the right (base density, base temperature, mass-loss rate, angular momentum-loss rate, open magnetic flux, and flux ratio between surface and open magnetic fluxes). Stellar parameters were compiled in Vidotto et al. (2014b). Distances are found using the Gaia DR2 database[a] (Prusti et al. 2016; Brown et al. 2018) values for parallax.

| | Observables | | | | | | Simulation | | | | | |
|---|---|---|---|---|---|---|---|---|---|---|---|---|
| Star | $M_\star$ ($M_\odot$) | $R_\star$ ($R_\odot$) | $P_{rot}$ (d) | $\Omega$ ($\Omega_\odot$) | Age (Gyr) | $d$ (pc) | $n_0$ ($cm^{-3}$) ($\times 10^8$) | $T_0$ (MK) | $\dot{M}$ ($M_\odot\ yr^{-1}$) ($\times 10^{-13}$) | $\dot{J}$ (erg) ($\times 10^{30}$) | $\Phi_{open}$ (G cm) ($\times 10^{22}$) | $f$ |
| $\chi^1$ Ori | 1.03 | 1.05 | 4.86 | 5.60 | 0.5 | $8.84^{\pm 0.02}$ | 18.9 | 2.84 | 46.5 | 285 | 22.5 | 0.37 |
| HD 190771 | 0.96 | 0.98 | 8.8 | 3.09 | 2.7 | $19.02^{\pm 0.01}$ | 13.2 | 3.04 | 36.1 | 91.0 | 23.46 | 0.59 |
| $\kappa^1$ Ceti | 1.03 | 0.95 | 9.3 | 2.92 | 0.65 | $9.15^{\pm 0.03}$ | 12.8 | 2.98 | 22.1 | 124 | 30.71 | 0.44 |
| HD 76151 | 1.06 | 0.98 | 15.2 | 1.79 | 3.6 | $16.85^{\pm 0.01}$ | 9.54 | 2.47 | 8.26 | 31.8 | 14.68 | 0.49 |
| 18 Sco | 0.98 | 1.02 | 22.7 | 1.20 | 3.0 | $14.13^{\pm 0.02}$ | 7.5 | 1.85 | 6.47 | 5.34 | 4.29 | 0.70 |
| HD 9986 | 1.02 | 1.04 | 23 | 1.18 | 4.3 | $25.46^{\pm 0.03}$ | 7.44 | 1.82 | 5.82 | 2.35 | 3.30 | 0.94 |
| Sun Min | 1.0 | 1.0 | 27.2 | 1 | 4.6 | – | 6.72 | 1.5 | 1.08 | 1.04 | 3.44 | 0.69 |
| Sun Max | 1.0 | 1.0 | 27.2 | 1 | 4.6 | – | 6.72 | 1.5 | 1.94 | 15.5 | 6.17 | 0.24 |

*Note*. [a] https://gea.esac.esa.int/archive/

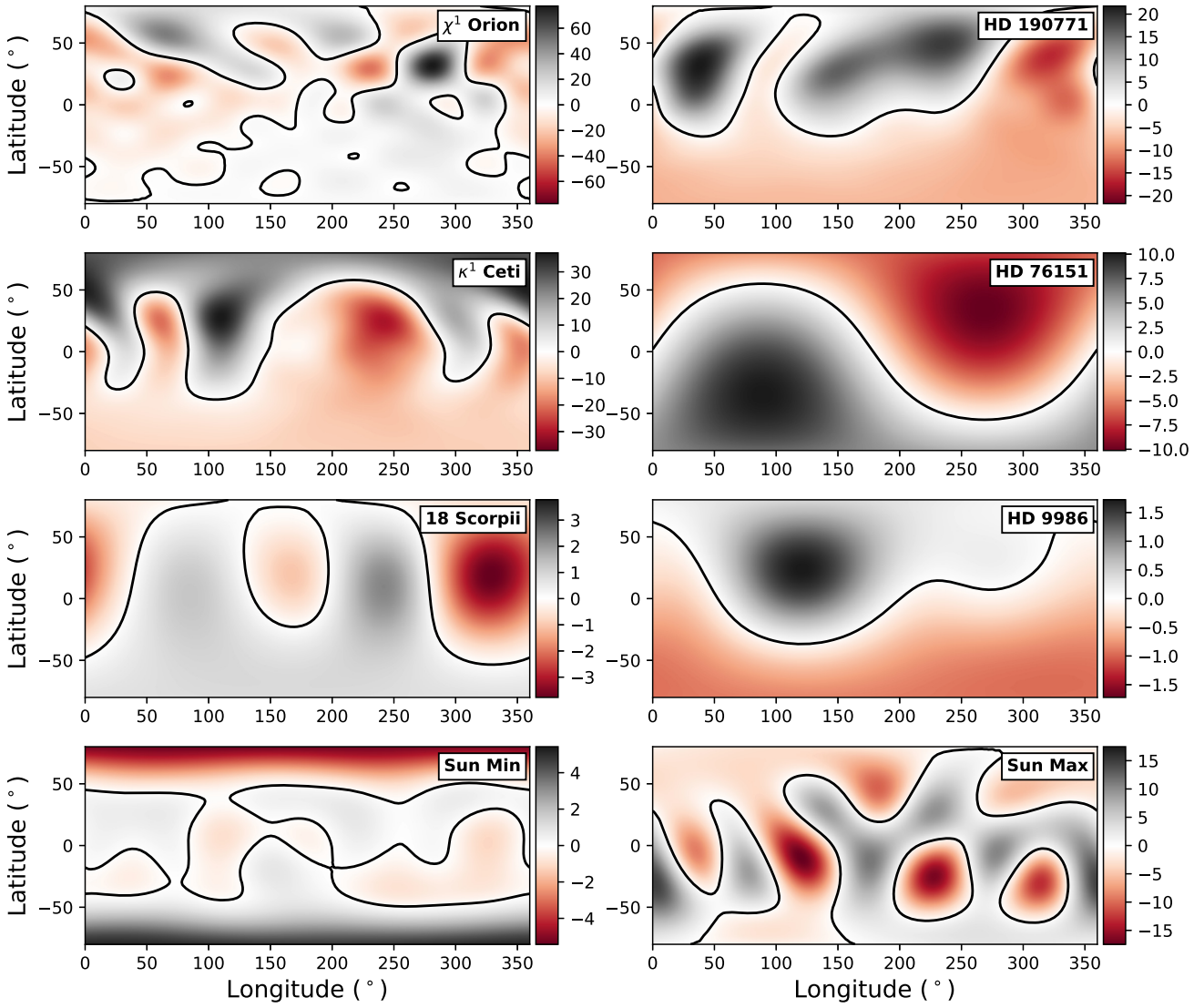


**Figure 1.** Radial surface magnetic fields of our stars. Each magnetic field is saturated at the maximum absolute value for each field respectively. Magnetic field contours are shown in Gauss. The maps are shown in latitude–longitude coordinates.

harmonic degrees, which is the most of all simulations. This star is the closest star in our sample at 8.84 pc.[2]

**HD 190771** This star possesses an uncharacteristically short rotation period (8.8 d) for its commonly used age (2.7 Gyr, derived from isochrone fitting, Valenti & Fischer 2005). This fast rotation should indicate a more active star, which we see validated in the ZDI observations of the magnetic field at the stellar surface. We see one of the least dipolar fields in the sample, with large areas of strong magnetic field of both polarities in the northern hemisphere (Fig. 1). Note that polarity reversal has been observed to occur in the magnetic field of this star (Petit et al. 2009).

**$\kappa^1$ Ceti** is estimated to be the second youngest star in our selected sample, with an age of 0.65 Gyr (Rosén et al. 2016). The observed rotation period from photometry is 9.2 d (Messina & Guinan 2003; Rucinski et al. 2004, ground and space, respectively). The higher levels of activity in this star are apparent when we examine the ZDI map, with non-dipolar geometry and relatively strong $B$ field ($B_{\rm r,max} \approx 35$ G, do Nascimento, Jr. et al. 2016). It is the second closest star in our sample (excluding the Sun), at a distance of 9.13 pc.[2]

**HD 76151** has a rotation period of 15.2 d (Maldonado et al. 2010). The age of HD 76151 is estimated to be 3.6 Gyr (Petit et al. 2008). ZDI observations of HD 76151 present a strong dipolar field, with $B_{\rm r,max} \approx 10$ G, which is tilted to the axis of rotation by 30° (Petit et al. 2008). Considering the age of the star and the dipolar geometry of the magnetic field, we expect a slower wind than the faster, more magnetically active rotators (see also Pognan et al. 2018) .

**18 Scorpii** is 3 Gyr old and possesses a rotation period of 22.3 d. It displays very quiescent behaviour, with a weak, largely dipolar magnetic field (Petit et al. 2008). It is the most similar solar twin for which we have surface magnetic field measurements, displaying very similar spectral lines to the Sun (Meléndez et al. 2014). Recently, many more solar twins have been identified (Lorenzo-Oliveira et al. 2018), however, these stars do not have magnetic field observations.

**HD 9986** presents another off axis dipole, with a maximum field strength of 1.6 G and an age of 4.3 Gyr (Vidotto et al. 2014b). This is the weakest magnetic field of any star in the sample, Petit et al. (in preparation).

**The Sun** has a well documented cyclical behaviour, of which we take one map at the maximum of the cycle, and another map at the minimum of the cycle. Maps for the minima and maxima are taken at Carrington rotations 1983 and 2078, respectively, which were observed with SOHO/MDI in the years 2001 and 2008. We have removed the higher degree harmonics ($\ell \geq 5$) for both maps, so as to replicate the Sun as if observed similarly to the other slowly rotating stars in the sample (Vidotto 2016; Lehmann et al. 2018; Vidotto et al. 2018). We note that the Sun at maximum possesses a much more complex magnetic geometry than the solar minimum, including a stronger magnetic field (e.g. DeRosa, Brun & Hoeksema 2010).

## 3 WIND MODELLING

### 3.1 3D numerical simulations of stellar winds

We use the 3D MHD numerical code BATS-R-US to simulate the winds of our sample of stars. This code has been used frequently in the past to study many magnetic astrophysical plasma environments (Powell et al. 1999; Tóth et al. 2005; Manchester et al. 2008; Vidotto et al. 2015; Vidotto 2017; Alvarado-Gómez et al. 2018). Here we use it to solve for eight parameters: mass density ($\rho$), wind velocity ($\boldsymbol{u} = \{u_x, u_y, u_z\}$), magnetic field ($\boldsymbol{B} = \{B_x, B_y, B_z\}$), and gas pressure $P$. The code numerically solves a set of closed ideal MHD equations representing, respectively, the mass conservation, momentum conservation, the induction equation, and the energy equation:

$$\frac{\partial \rho}{\partial t} + \nabla \cdot (\rho \boldsymbol{u}) = 0, \tag{1}$$

$$\frac{\partial (\rho \boldsymbol{u})}{\partial t} + \nabla \cdot \left[ \rho \boldsymbol{u}\boldsymbol{u} + \left( P + \frac{B^2}{8\pi} \right) \mathbf{I} - \frac{\boldsymbol{B}\boldsymbol{B}}{4\pi} \right] = \rho \boldsymbol{g}, \tag{2}$$

$$\frac{\partial \boldsymbol{B}}{\partial t} + \nabla \cdot (\boldsymbol{u}\boldsymbol{B} - \boldsymbol{B}\boldsymbol{u}) = 0, \tag{3}$$

$$\frac{\partial \varepsilon}{\partial t} + \nabla \cdot \left[ \boldsymbol{u} \left( \varepsilon + P + \frac{B^2}{8\pi} \right) - \frac{(\boldsymbol{u} \cdot \boldsymbol{B})\boldsymbol{B}}{4\pi} \right] = \rho \boldsymbol{g} \cdot \boldsymbol{u}, \tag{4}$$

where the total energy density is given by

$$\varepsilon = \frac{\rho u}{2} + \frac{P}{\gamma - 1} + \frac{B^2}{8\pi}. \tag{5}$$

Here, $\mathbf{I}$ denotes the identity matrix, and $\boldsymbol{g}$ the gravitational acceleration. We assume that the plasma behaves as an ideal gas, that $P = nk_{\rm B}T$, where $n = \rho/(\mu m_{\rm p})$ is the total number density of the wind, $\rho$ representing the mass density, and $\mu m_{\rm p}$ denoting the average particle mass. We take $\mu = 0.5$, which represents a fully ionized hydrogen wind. We can also relate the pressure to the density, by assuming the wind is polytropic in nature, which follows the relationship: $P \propto \rho^{\gamma}$, where $\gamma$ represents the polytropic index. This polytropic index implicitly adds heat to the wind as it expands, meaning we do not require an explicit heating equation in our model. We adopt $\gamma = 1.05$, which is similar to effective index found by Van Doorsselaere et al. (2011) for the Sun, and to values used in the literature for simulating winds (Vidotto et al. 2015; Pantolmos & Matt 2017; Ó Fionnagáin & Vidotto 2018).

The free parameters of polytropic wind models, such as ours, are the base density ($\rho_0$) and temperature ($T_0$) of the wind. Here, we use the empirical model from Ó Fionnagáin & Vidotto (2018) that relates both the temperature and density of the wind base with the rotation of the star (see also Holzwarth & Jardine 2007; See et al. 2014; Johnstone et al. 2015a,b; Réville et al. 2016).

$$T_0 \, (\Omega < 1.4 \, \Omega_\odot) = 1.5 \pm 0.19 \left( \frac{\Omega_\star}{\Omega_\odot} \right)^{1.2 \pm 0.54} \text{MK} \tag{6}$$

$$T_0 \, (\Omega > 1.4 \, \Omega_\odot) = 1.98 \pm 0.21 \left( \frac{\Omega_\star}{\Omega_\odot} \right)^{0.37 \pm 0.06} \text{MK} \tag{7}$$

$$n_0 = 6.72 \times 10^8 \left( \frac{\Omega_\star}{\Omega_\odot} \right)^{0.6} \text{cm}^{-3}. \tag{8}$$

To set the magnetic field vector, we use the radial component of the ZDI maps at the stellar surfaces (Fig. 1). At the initial state, we use a potential field source surface model (e.g. Altschuler & Newkirk 1969) to extrapolate the magnetic field into the grid, with the field lines becoming purely radial beyond 4 $R_\star$. The code then numerically solves the MHD equations and allows the magnetic

[2] https://gea.esac.esa.int/archive/

field to interact with the wind (and vice versa), until it reaches a relaxed state.

Fig. 2 shows the structure of the winds, with open magnetic field lines displayed in grey and closed magnetic fields shown in red. We can see the field lines become much more structured and organized in the slower rotators with more dipolar fields, as opposed to the complex field lines of the faster rotators with less dipolar fields. Equatorial radial velocities are shown as a yellow-blue graded surface, with the radial velocities ranging from 300 to 580 km s$^{-1}$ at 0.1 au, near the outer boundary of our simulations. Shown in orange are the Alfvén surfaces, which denote where the poloidal wind velocity equals the Alfvén velocity ($u_{\rm pol} = u_A = B/\sqrt{4\pi\rho}$). They display where the wind becomes less magnetically dominated and more kinetically dominated by the flowing wind. We see these Alfvén surfaces range from 2 to 6 R$_\star$ across our sample. Stars with very weak magnetic fields (e.g. 18 Sco, HD 9986) generally have smaller Alfvén surface radii.

### 3.2 Mass-loss rates ($\dot{M}$), angular momentum-loss rates ($\dot{J}$), and open magnetic flux ($\Phi_{\rm open}$)

From our wind simulations we can calculate the mass-loss rate from each of the stars by integrating the mass flux through a spherical surface $S$ around the star

$$\dot{M} = \oint_S \rho u_r \, {\rm d}S, \tag{9}$$

where $\dot{M}$ is the mass-loss rate, $\rho$ is the wind density, $u_r$ is the radial velocity, and $S$ is our integration surface. In our simulations we see an overall decrease of $\dot{M}$ with decreasing rotation rate, Table 1, which is consistent with the works of Cranmer & Saar (2011), Suzuki et al. (2013), Johnstone et al. (2015a,b), and Ó Fionnagáin & Vidotto (2018). We note that the mass-loss rate we find for the Sun is ∼5 times larger than the observed value of $\sim 2 \times 10^{-14}$ M$_\odot$ yr$^{-1}$. This is because of our choice of base density, which is three times higher than in Ó Fionnagáin & Vidotto (2018). We opted for a three times higher base density as we were unable to find a stable solution for the winds of a few stars in our sample. Ó Fionnagáin & Vidotto (2018) suggested that the angular-momentum loss for solar-type stars would drop off substantially for slow rotators, causing older solar-type stars to rotate faster than expected. This would explain the findings of Van Saders et al. (2016), who observed a set of ageing solar-like stars and discovered that they rotated at much faster rates than expected by the traditional Skumanich age–rotation relationship. In our previous work, Ó Fionnagáin & Vidotto (2018), we linked the anomalous fast rotation at older ages to the drop in mass-loss rates at older ages, and consequently, to a drop in the angular momentum-loss rate. Unfortunately, we could not verify this drop in angular momentum for slower rotators, as we do not have magnetic field maps for solar-mass stars that rotate much slower than the Sun. This lack in magnetic field maps in this regime can be explained observationally as detecting weak magnetic fields in slowly rotating stars is very challenging. Therefore, we compare mass-loss rates calculated here using the faster rotators. Fig. 3 shows the mass-loss rate (red points) and the fit to these points (red line) which follows the relationship

$$\dot{M} = 4.7(\pm 0.1) \times 10^{-13} \left(\frac{\Omega_\star}{\Omega_\odot}\right)^{1.4\pm0.2} {\rm M}_\odot \, {\rm yr}^{-1}. \tag{10}$$

The fit to the faster rotators from Ó Fionnagáin & Vidotto (2018) (shown as a dotted black line), which possesses the power-law index of 1.4, agrees within the error to the power law index fit here of $1.6 \pm 0.2$. It is interesting that these mass-loss rates agree so well considering the base density of the 3D simulations is three times higher than in Ó Fionnagáin & Vidotto (2018). This suggests that the inclusion of a magnetic field in the 3D simulations would generate a much lower mass-loss rate than in the 1D simulations, given the same base densities. This is most likely due to closed magnetic regions, which act to hold in material, and reduce $\dot{M}$.

We also determine $\dot{J}$ from our simulations as

$$\dot{J} = \oint_S \left[ -\frac{\varpi B_\phi B_r}{4\pi} + \varpi u_\phi \rho u_r \right] {\rm d}S, \tag{11}$$

where $\varpi = (x^2 + y^2)^{1/2}$, the cylindrical radius, $B$ and $u$ are the magnetic field and velocity components of the wind, and $r$ and $\phi$ denote the radial and azimuthal components, respectively (Mestel 1999; Vidotto et al. 2014a). The integral is performed over a spherical surface ($S$) in a region of open field lines. From Fig. 3 we see a trend of decreasing $\dot{J}$ towards slower rotating stars. We note that while the solar minimum simulation has a reasonable angular momentum loss rate, we find that the solar maximum simulation has a higher $\dot{J}$ than expected (see e.g. Finley et al. 2018).

The magnetic field geometry and strength affect the wind in these simulations as it evolves, by establishing a pressure and tension against the ionized plasma. Here we calculate how much of the wind consists of open and closed field lines, by integrating the unsigned magnetic flux passing through a surface near the outer edge of our simulation domain, where all the field lines are open

$$\Phi_{\rm open} = \oint_{S_{\rm sph}} |B_r| \, {\rm d}S. \tag{12}$$

The open flux of the wind, $\Phi_{\rm open}$, is relevant as regions of open flux the origin of the fast solar/stellar wind (Verdini et al. 2010; Réville et al. 2016; Cranmer, Gibson & Riley 2017). It is also related to how efficient the wind is at transporting angular momentum from the star (Réville et al. 2015). In Fig. 3 we see that across the rotation periods of our sample, open flux decreases as the stars spin-down. There is also a hint of an open flux plateau in the faster rotators. In Table 1, we also present the ratio $f$ of open to unsigned surface magnetic field flux ($\Phi_{\rm surf}$), following the convention: $\Phi_{\rm surf} = f\Phi_{\rm open}$.

### 3.3 Wind derived properties at typical hot-Jupiter distances

From our simulations we can gather much information on the structure of the winds of solar-like stars. This aids us in the analysis of the wind evolution from young to older solar-type stars along the main sequence. It also impacts the study of exoplanet evolution, as exoplanets exist orbiting these stars, embedded in the stellar wind. The main components of the wind affecting exoplanets are magnetic pressure (for close in exoplanets) and ram pressure (for distantly orbiting exoplanets). There also exists a thermal pressure constituent to the wind, but this is usually much smaller than both of the previous pressures. In our case, at 0.1 au the ram pressure dominates as this is well above the Alfvén surface for each star. The ram pressure is given as

$$P_{\rm ram} = \rho u_r^2. \tag{13}$$

Here we assume the orbit to be in the equatorial plane aligned with the rotation axis, but we note that this might not always be the case for hot Jupiters (Huber et al. 2013; Anderson, Storch & Lai 2016). We see from Fig. 4 that there can be large variations

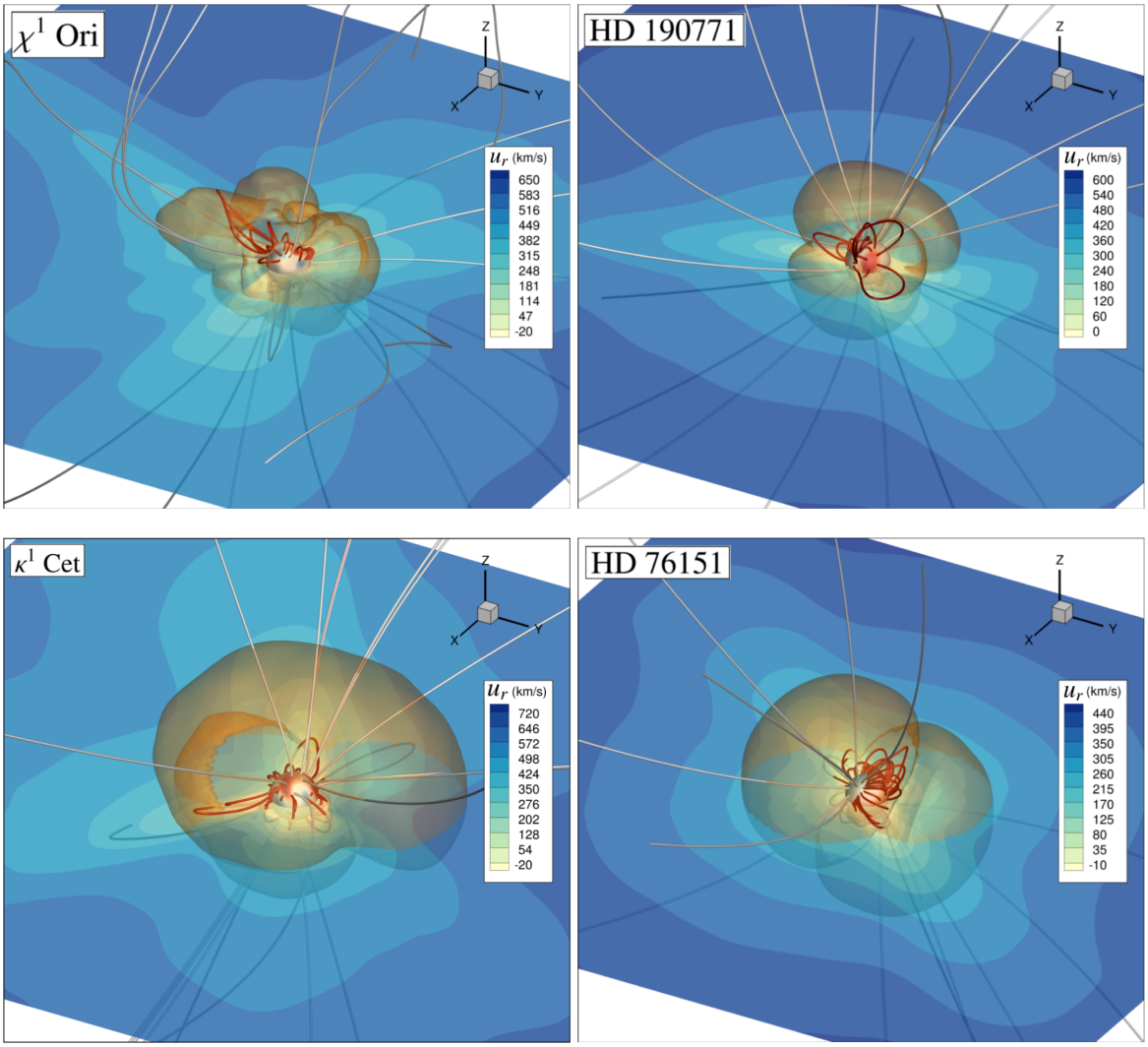


**Figure 2.** Steady state solutions for the simulated winds of the solar analogues. The translucent slice through the $z = 0$ plane shows the wind radial velocity ($u_r$). Open and closed magnetic field lines are shown as grey and red streamlines, respectively. Magnetic polarity is shown on the stellar surface as a red-blue diverging contour. The orange surface shows the Alfvén surface, where $u_r = u_A$, the Alfvén velocity. Note that the faster rotators have much less uniform, dipolar Alfvén surfaces, due to the less uniform magnetic fields topologically, at their surfaces.

in the ram pressure impinging upon an orbiting exoplanet at 0.1 au, both within a single orbit around a particular host star, and between each host star. From these, we infer the evolution of the planetary environment around a solar-like star as it evolves. We see that the Sun at minimum possesses the lowest ram pressure of any of the stars in our sample. We can compare the distribution of velocities for all of the stars by histogramming the velocities across a sphere of 0.1 au. This method can give insight into the structure of the wind, discerning uni-modal and multimodal wind structures (see Fig. 5). We observe that more complex and stronger fields lead to less uniform wind structures. We can see that the winds of 18 Sco, HD 9986, and the Sun at minimum display unimodality, while other stars such as $\chi^1$ Ori and HD 190771 have a very skewed velocity distributions. The magnetic field strength and geometry seems to directly affect the wind structure even at these distances. This is discussed in Réville et al. (2016), who noted that the expansion of magnetic flux tubes can cause an acceleration in the wind.

## 4 RADIO EMISSION OF THE SOLAR WIND IN TIME

### 4.1 Radiative transfer model

It has long been established that the plasma of stellar winds emit at radio wavelengths through thermal free–free processes (Panagia & Felli 1975; Wright et al. 1975; Lim & White 1996). If this radio emission is observed, it could provide a way to detect the winds of low-mass stars directly, allowing an estimation of the wind density and temperature at that location in the wind. Constraining the density of the wind would allow a much better estimate on the mass-loss rate of the star, and by extension angular-momentum loss rates.

Analytical expressions for the radio emission calculation are commonly used in the literature (Panagia & Felli 1975; Wright et al. 1975; Lim & White 1996; Fichtinger et al. 2017; Vidotto & Donati 2017). For example, Panagia & Felli (1975) assumed a power law dependence of density with radial distance, such that

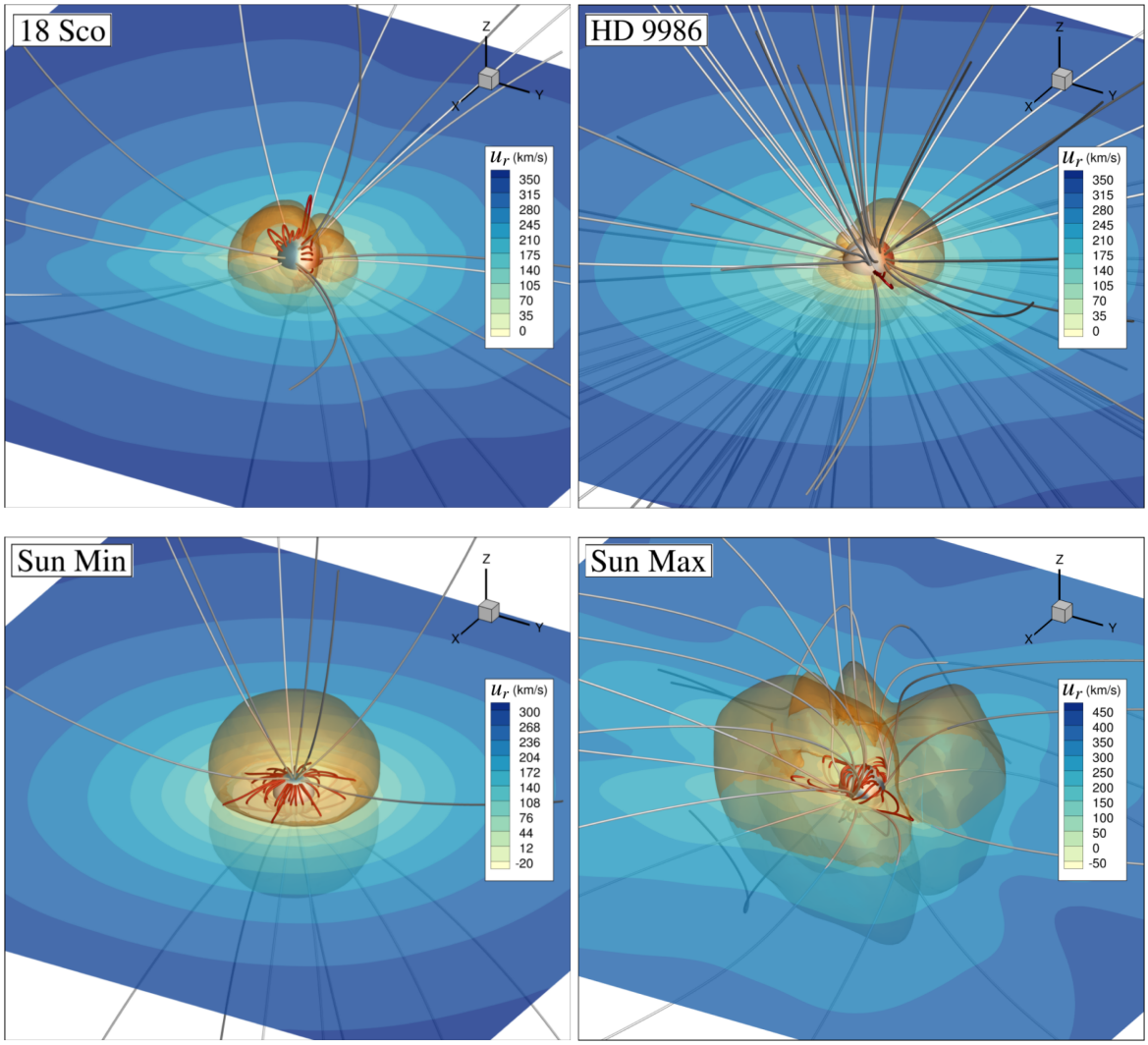


**Figure 2.** Continued.

$\rho \propto R^{-\alpha}$, which generates a radius dependence for radio flux density with frequency: $S_\nu \propto \nu^{\frac{-4.2}{2\alpha-1}+2}$. However, when $R$ is small and the wind is still accelerating, this density dependence deviates from a power law. Thus, these power-law gradients can underestimate the density decay close to the star and overestimate it further from the star. This is discussed further in Appendix A. A similar approach is also used in defining the distance-dependence of the temperature of the wind. To overcome this, we perform the radio emission calculation from first principles, by solving the radiative transfer equation numerically (code available on GitHub: https://github.com/ofionnad/radiowinds; Ó Fionnagáin 2018). Using our 3D MHD simulations, we can use the exact density decay expected, which gives a more precise estimation of the wind emission.

Fig. 6 shows a schematic of our calculation grid, we divide the grid into equally spaced cells, each possessing a value of wind density and temperature. The illustration shows a red annulus around a magnetic star, outlining the expected radio emission from the wind (this is not expected to be spherically symmetric). Note that the actual number of cells used in calculations ($=200^3$) is much greater than depicted in Fig. 6. From this, we can calculate the thermal emission expected from these winds by solving the radiative transfer equation,

$$I_\nu = \int_{-\infty}^{\tau'_{\rm max}} B_\nu \mathrm{e}^{-\tau}\, \mathrm{d}\tau' \tag{14}$$

where $I_\nu$ denotes the intensity from the wind, $B_\nu$ represents the source function, which in the thermal case becomes a blackbody function, $\tau$ represents the optical depth of the wind, with $\tau'$ representing our integration coordinate across the grid. The optical depth of the wind depends on the absorption coefficient, $\alpha_\nu$, of the wind as

$$\tau_\nu = \int \alpha_\nu \mathrm{d}s, \tag{15}$$

where $s$ represents the physical coordinate along the line of sight, $\alpha_\nu$ is described as (Panagia & Felli 1975; Wright et al. 1975; Cox & Pilachowski 2002),

$$\alpha_\nu = 3.692 \times 10^8 [1 - \mathrm{e}^{-h\nu/k_\mathrm{B}T}] Z^2 f_\mathrm{g} T^{-0.5} \nu^{-3} n_\mathrm{e} n_\mathrm{i} \tag{16}$$

and the blackbody function is the standard Planck function.

$$B_\nu = \frac{2h\nu^3}{c^2} \frac{1}{\mathrm{e}^{h\nu/k_B T} - 1}, \tag{17}$$

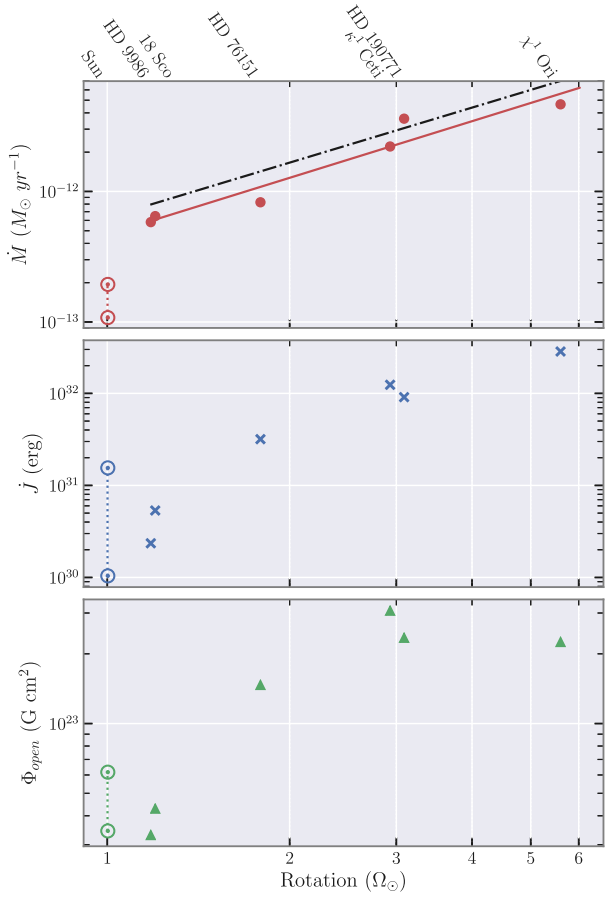


**Figure 3.** Top to bottom, the three panels above show the mass-loss rate, angular momentum-loss rate, and unsigned magnetic open flux from our sample of simulations. The stars are labelled at the top of the figure, with the solar simulations represented by the solar symbol (⊙), where activity maximum is always on top. In the top panel we include a fit to the data (red line, excluding the Sun) and compare this to the fast rotator fit as described in Ó Fionnagáin & Vidotto (2018) (black dashed line).

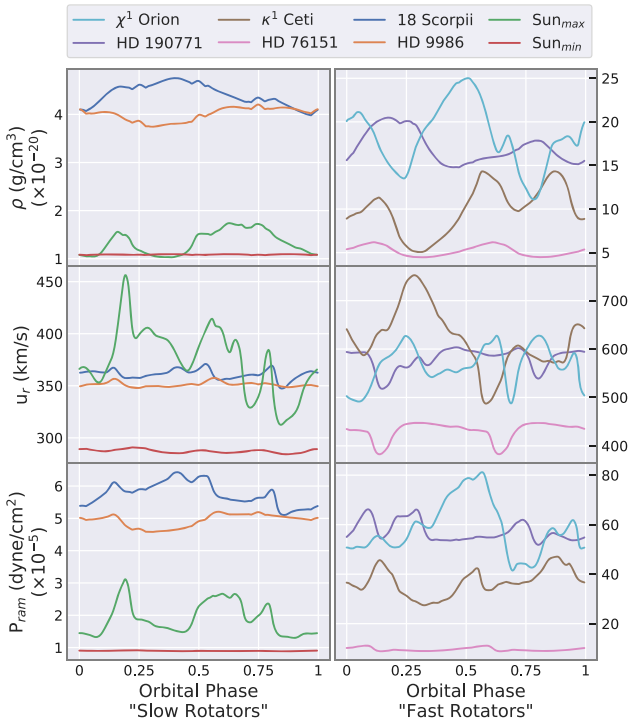


**Figure 4.** *Top:* Figure showing the density variations of the wind at the equator ($z = 0$ plane) for each star in our sample, at a distance of 0.1 au. *Middle:* The velocity variations of the wind at the equator at 0.1 au. *Bottom:* Calculated ram pressures of the wind at 0.1 au at the equator, using equation (13). The figures are split into slow (left) and fast (right) rotators so to conserve the visibility of variation across all winds. Note that the $y$-axes on the left and right have different scales. This figure is optimally viewed in colour.

where $\nu$ is the observing frequency, $h$ is Planck's constant, $k_B$ is Boltzmann's constant, $T$ is the temperature of the wind, $Z$ is the ionic state of the wind (+ 1 for our ionized hydrogen wind), with $n_e$ and $n_i$ representing the electron and ion number densities of the wind. In our case we have the same number of ions and electrons, so this becomes simply $n_i^2$. $f_g$ is the gaunt factor which is defined as (Cox & Pilachowski 2002)

$$f_g = 10.6 + 1.9 \log_{10} T - 1.26 \log_{10} Z\nu. \quad (18)$$

### 4.2 Evolution of the radio emission with age

Using equations (14) or (17) we calculate 2D images for each frequency (cube of data) for the intensity and optical depth, across the plane of the sky, showing the intensity attributed to different regions of the wind, and the optical depth associated with it. This is represented in Fig. 7. Note that for comparison we calculate solar wind radio emission at a distance of 10 pc. We can see that the intensity of the emission increases as we increase the frequency, although it radiates from a much smaller region. This is due to the decrease in the optical depth with frequency and allows us to see further into the wind, to much denser regions giving rise to more emission. The optical depth of the wind will have a major impact on the observations of these winds. Low optical depths allow emission from the low corona to escape and be detected, these regions are contaminated with other forms of radio emission, likely dominant, such as chromospheric emission and flaring. However, Lim & White (1996) suggest that we still can provide meaningful upper limits to the mass-loss rate of the star if a flare is detected as one must assume a maximum base density to the wind, therefore constraining mass-loss rates. From the intensity we can calculate the flux density ($S_\nu$) of the wind as

$$S_\nu = \frac{1}{d^2} \int I_\nu \, dA = \frac{1}{d^2} \sum^{i,j} I_\nu \, \Delta i \, \Delta j, \quad (19)$$

where $A$ is the area of integration, $d$ is the distance to the object, and $i$ and $j$ denote the coordinates in our 2D image of $I_\nu$ values. $\Delta i$ and $\Delta j$ represent the spacing in our grid in the $i$ and $j$ directions. In this calculation we have assumed that the angle subtended by the stellar wind is small, therefore $d\Omega = dA/d^2$.

Table 2 shows the main results from our radio emission calculation, giving values for the expected flux density, from each star at 6 GHz. Fig. 8(a) shows the spectrum of each stellar wind for the range of frequencies 0.1–100 GHz. Our calculation uses actual density distribution in the simulated wind to find the optical depth and the flux density. We obtain a spectrum in the optically thick regime, leading to a power law fit which is related to the density gradient in the wind. Another result of using a numerical model is that the radio photosphere ($R_\nu$), calculated at a distance where $\tau = 0.399$, is not spherical, but changes with the density variations in the wind, causing anisotropic emission, as evident from Fig. 7

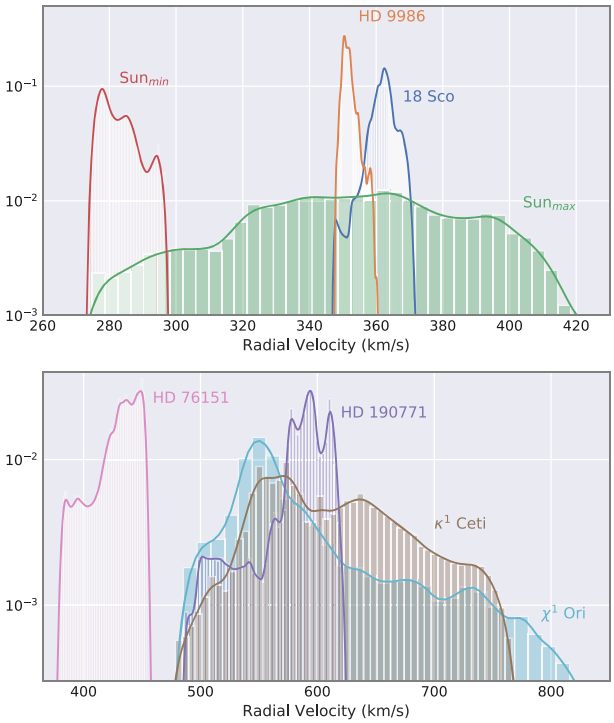


**Figure 5.** Velocity histogram for our stellar sample, allowing insight into the wind structure (e.g. Réville et al. 2016). Velocities are taken at a distance of 0.1 au, and split into slower rotators (top) and faster rotators (bottom). Note the different velocity scales on each panel. This histogram shows the normalized frequency of each velocity present in the wind at this distance. We can see that the winds of 18 Sco and HD 9986 are extremely unimodal, while other stars such as HD 190771 have a very skewed distribution of velocities. The magnetic field strength and geometry seems to directly affect the wind structure even at these distances. Bin size is selected using the Freedman–Diaconis rule.

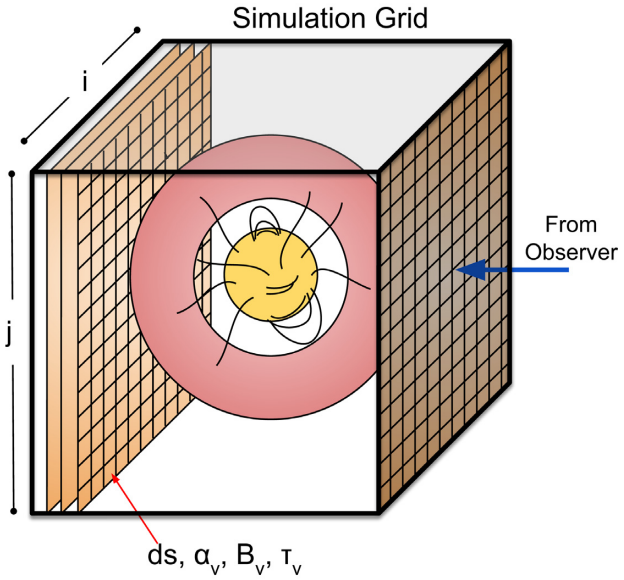


**Figure 6.** Schematic showing how the intensity is calculated from our grid. The red annulus around the star illustrates thermal radio emission regions from the wind, with a magnetic star at the centre of the diagram. From our wind simulation we create a grid of uniform discrete distances filled with variables including position ($s$), density ($n$), and temperature ($T$). From this we calculate values for the absorption coefficient ($\alpha$, equation 16), the blackbody function ($B_\nu$, equation 17), and the optical depth ($\tau_\nu$, equation 15) for each cell in our grid. We integrate along the line of sight from the observer to find the intensity using equation (14), and find flux density by integrating across $i$ and $j$. We take the line of sight to be along the $x$ axis for each star, which is not necessarily true, but adopted as such because it is assumed variability in the radio emission will not vary much depending on viewing angle or rotation axis.

(dashed contours). Note that these radio winds are not resolvable with current radio telescopes but should indicate how the radio photosphere in the wind changes with frequency, and the anisotropy of the specific intensity, $I_\nu$, in the wind. We also provide a power-law fit to the optically thick regime of the radio emission (from 0.1 to 1 GHz) and note that it can vary quite significantly, depending on what range of frequencies is being fitted. In Table 2 we show the fit parameters we find according to

$$S_\nu = S_0 \nu^\phi. \tag{20}$$

Our radio calculations give an insight into the expected emissions from solar-type stars. We see that, at the appropriate sensitive frequencies for radio telescopes such as the VLA, the winds all exhibit similar spectrum shapes. Fig. 8(a) shows the spectrum for each star, using different colours as depicted in the legend. We show that the upper limits set by Fichtinger et al. (2017) (hereafter, F17) (black arrows) are consistent with our estimations of the wind emission for $\kappa^1$ Ceti: our values are three times lower than these upper limits. $\chi^1$ Ori is detected by F17, but they attribute this emission to the chromosphere and other sources as the star was observed to flare during the observation epoch (we discuss detection difficulties further in Section 4.4). Indeed, Fig. 8(a) shows the detected emission occurs within the optically thin regime of the spectrum according to our models and at approximately 20 times higher flux density than we predict for the stellar wind emission. This supports the deduction that these detections are from other sources, and not the thermal wind. F17 estimated the thermal wind emission to possess a flux of 1.3 μJy at 10 GHz, which agrees quite well with our calculation of 0.77 μJy. If the emission seen at 100 μJy by F17 were coming from the stellar wind, our models would require a base density five times larger ($\approx 10^{10}$cm$^{-3}$). With this, we can actually infer that the mass-loss rate of $\chi^1$ Ori is smaller than 2–3 $\times 10^{-11}$ M$_\odot$ yr$^{-1}$, showing that even non-detections of stellar wind radio emission can still provide meaningful upper limits for the mass-loss rates. If we normalize the spectra shown in Fig. 8(a) to remove the distance dependence, upon which the spectrum relies very heavily, we see that the younger more rapidly rotating stars display a higher flux density than the more evolved stars. The Sun in this case would possess the weakest emission.

### 4.3 Evolution with magnetic cycle

In Fig. 8(a) we calculate the expected radio emission from our solar maximum and solar minimum simulations assuming a distance of 10pc (grey lines) to give an impression of the differences between the radio emission of the winds and the detectability of each star. We show that the thermal quiescent radio flux does not change substantially across a solar magnetic cycle. This is because the radio emission is heavily dependent on the density of the medium and both solar simulations have the same base density. The slight spectral differences, which occur mostly in the optically thick regime, are a consequence of the different magnetic fields causing different density gradients in the wind. For there to be substantial differences

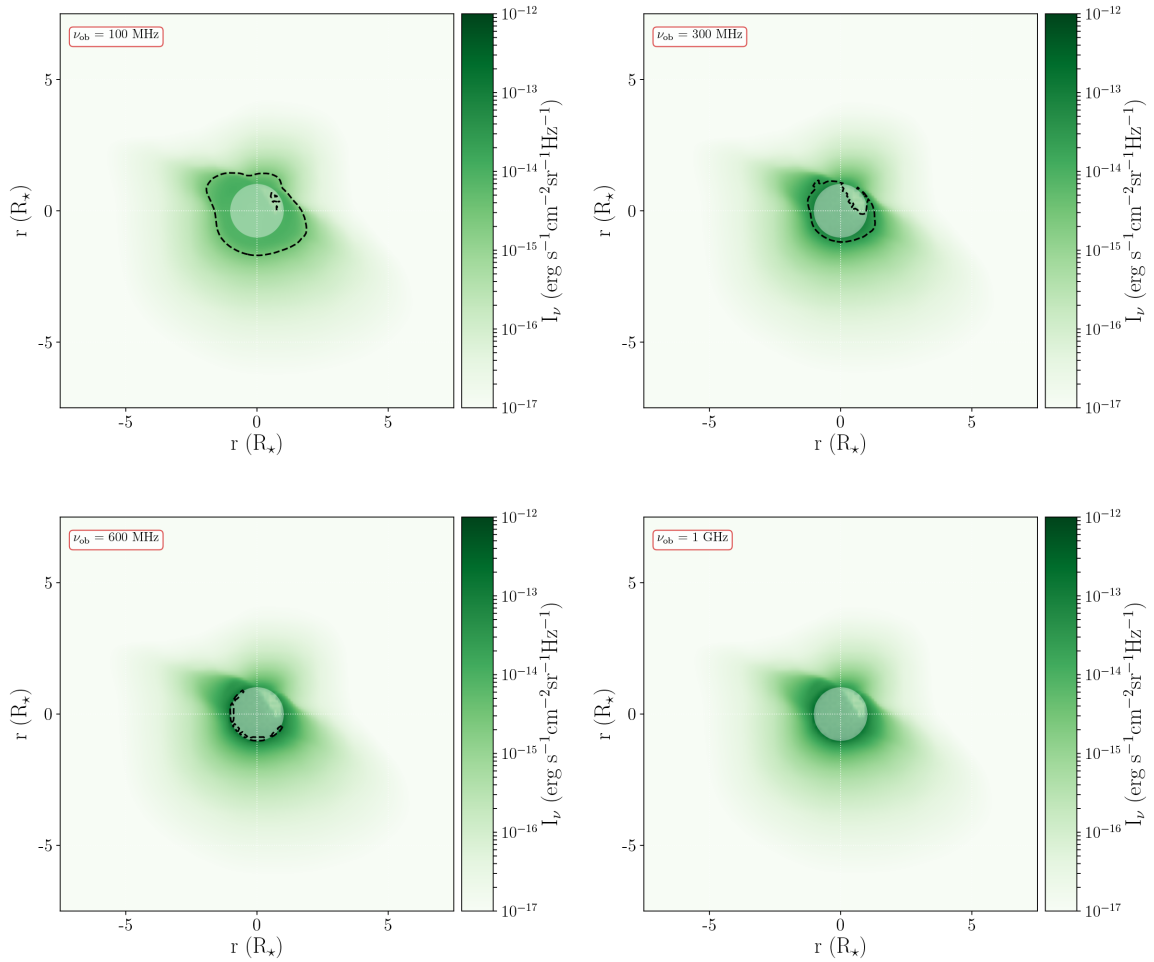


**Figure 7.** Example of intensity and optical depth for $\kappa^1$ Ceti at observing frequencies of 100 MHz (top left), 300 MHz (top right), 600 MHz (bottom left), and 1 GHz (bottom right). The green colour scale represents the intensity of emission from the wind, looking along the line of sight of our simulation grid. The dashed black contour represents the region where the wind becomes optically thick [according to Panagia & Felli (1975), $\tau = 0.399$]. We can see that the emission is anisotropic due to the anisotropy of the wind density and temperature. The intensity reaches a maximum in the thin regime, as we can see emission from the entire wind. The white circle denotes $R = 1$ R$_\star$. There exists no contour in the bottom right plot as the wind is optically thin at 1 GHz. Plasma in front of the star still emits in radio, but we have excluded any contribution from behind the star along the line of sight.

**Table 2.** Predicted radio emission from our stellar wind models. Example fluxes at a frequency of 6 GHz are given ($S_{6\mathrm{GHz}}$), in this case we find that all of the winds would be optically thin at this frequency. The power-law fit to the spectra was conducted between 0.1 and 1 GHz, giving the coefficient ($S_0$) and power index ($\phi$). However, the spectral slope between these two frequencies varies substantially, tending to shallower slopes at higher frequencies. Depending on the fitting range, slopes can range from 0.6 to 1.5. All slopes tend to −0.1 in the thin regime. The final columns gives the frequency at which each wind becomes optically thin ($\nu_{\mathrm{thin}}$).

| Star | $S_{6\mathrm{GHz}}$ (μJy) | $S_0$ | $\phi$ | $\nu_{\mathrm{thin}}$ (GHz) |
|---|---|---|---|---|
| $\chi^1$ Ori | 1.75 | 1.53 | 1.32 | 1.93 |
| HD 190771 | 0.19 | 0.19 | 1.13 | 1.67 |
| $\kappa^1$ Ceti | 0.79 | 0.81 | 1.14 | 1.93 |
| HD 76151 | 0.14 | 0.16 | 1.11 | 2.22 |
| 18 Sco | 0.14 | 0.16 | 1.10 | 1.93 |
| HD 9986 | 0.04 | 0.05 | 1.12 | 1.93 |
| Sun max (10 pc) | 0.22 | 0.26 | 1.21 | 2.10 |
| Sun min (10 pc) | 0.22 | 0.25 | 1.14 | 2.10 |

in thermal radio emission from a star displaying cyclic magnetic behaviour there would need to be a dramatic change in global density at the base of the wind. Note that the emission calculated here is quiescent wind emission and is the same in both the solar maximum and minimum cases. Non-thermal radio emission, such as 10.7 cm emission, is linked to solar activity and varies through the solar activity cycle (Solanki, Inhester & Schüssler 2006).

### 4.4 Detectability

The density at low heights in the stellar atmosphere is much higher than the stellar wind density. Radio emission from the lower atmosphere should dominate the emission in the optically thin regime of the stellar wind. This would most likely drown out any emission from the wind in the upper atmosphere and make detection of the wind impossible. However, as pointed out by Reynolds (1986), if the wind is entirely optically thin and emission is deduced to emanate from the lower stellar atmosphere, this can aid in placing limits on the stellar winds density and therefore the mass-loss rate of the star (cf. end of Section 4.2).

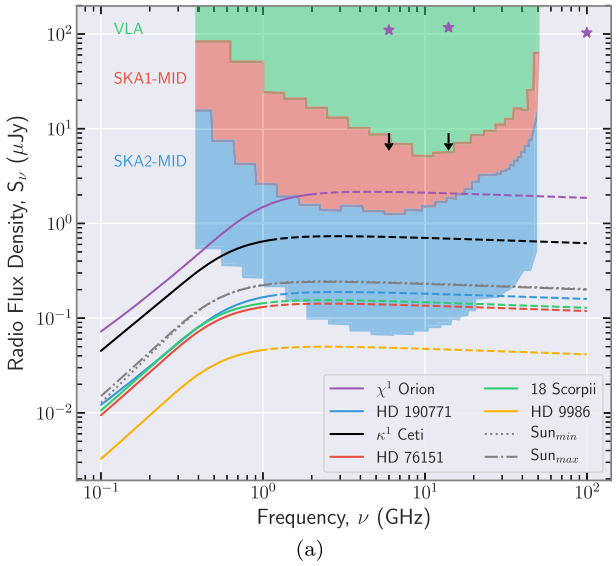


**Figure 8.** *Top:* We see that the radio spectra for each wind are very similar in shape. Differences in flux density are strongly affected by distance to the object. The dashed lines represent the optically thin part of each spectrum, and there are differences in where the emission becomes optically thin from star to star at the frequency $\nu_{\rm thin}$. The black arrows indicate the observational upper limits of $\kappa^1$ Ceti found by Fichtinger et al. (2017). From the same work we mark the chromospheric detections of $\chi^1$ Ori (purple stars), using both VLA and ALMA, which is concluded to originate from chromospheric emission. Our results show this conclusion to be valid as we predict the wind to emit at much lower fluxes. Sensitivities of the current VLA and future SKA1-MID and SKA2-MID are included shaded in green, red, and blue, respectively (SKA sensitivities from Pope et al. 2018) and adjusted for 2 h integration time. *Bottom:* Here we normalized spectra in the top panel to a distance of 10 pc. This allows direct comparison of radio emission to an ageing solar wind. As the stars age and spin-down the radio emission decreases by an order of magnitude between 500 Myr and 4.6 Gyr.

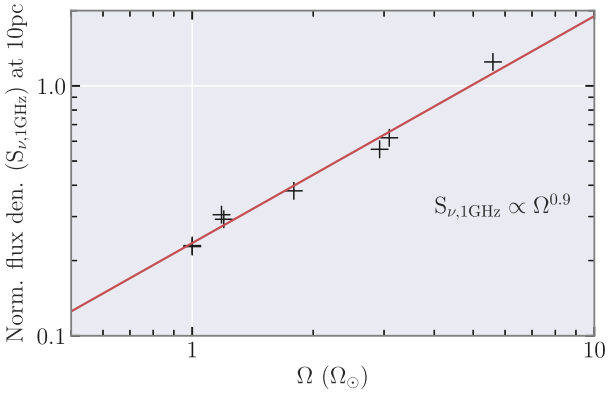


**Figure 9.** Normalized flux density at 1 GHz as a function of stellar rotation. We see a tight fit to this power law (see equation 21), with an almost linear dependence of stellar wind radio flux on stellar rotation at 1 GHz.

There have been many observations of solar-type low-mass stars in the radio regime (Güdel et al. 1998; Gaidos et al. 2000; Villadsen et al. 2014; Fichtinger et al. 2017), many of which have placed upper flux densities and mass-loss rates on the winds of these stars. Both Gaidos et al. (2000) and F17 used the VLA to observe a set of solar analogues, some of which overlap with the stars we have simulated here, placing tight constraints on the wind of $\kappa^1$ Ceti. Fig. 8(a) displays the sensitivity of the VLA (purple shade) given some typical observational parameters (2 h integration time, 128 MHz bandwidth) taken at central band frequencies. We show that the VLA is currently not sensitive enough to detect the winds simulated here. Villadsen et al. (2014) observed four nearby solar-like stars using the VLA (X, Ku, and Ka bands, at 10, 15, and 34.5 GHz centre frequencies, respectively). The authors find detections for all objects in the Ka band but can only provide upper limits to flux density for the other frequency bands. They conclude (similarly to F17) that all detections come from thermal chromospheric emission, and the upper limits set at lower frequencies infer rising spectra and so optically thick chromospheres at these frequencies.

In the future, upgrades to the existing VLA system (ngVLA, see Osten et al. 2018) could increase instrument sensitivity by a factor of 10. This increase in sensitivity means that stars simulated here such as $\chi^1$ Ori and $\kappa^1$ Ceti would be detectable in their thin regime. The Square Kilometre Array (SKA) project is a future low-frequency radio telescope that will span a large frequency range. The expected sensitivity level of the future SKA1-MID and SKA2-MID telscopes (with a typical 2 h integration time[3]) are shown in Fig. 8(a), shaded in red and blue (sensitivities for SKA taken from Pope et al. 2018, but adjusted to account for a 2 h integration time). Given these sensitivities one could potentially directly detect the winds of $\chi^1$ Ori and $\kappa^1$ Ceti using the SKA, below 1 GHz. This sensitivity level (sub-μJy) means other possible solar analogues not simulated here could also be detected, provided they are close enough. First light for SKA1-MID is expected after the mid 2020's.

We show in Fig. 8(b) that the faster rotators emit more flux. In Fig. 9, we present the normalized flux density at 1 GHz and at a

[3]https://astronomers.skatelescope.org/wp-content/uploads/2016/05/SKA-TEL-SKO-0000002_03_SKA1SystemBaselineDesignV2.pdf

distance of 10pc as a function of rotation rate. We found that

$$S_{\nu,1\,\mathrm{GHz}} = 0.24 \left[\frac{\Omega}{\Omega_\odot}\right]^{0.9} \left[\frac{10\,\mathrm{pc}}{d}\right]^{2} \mu\mathrm{Jy}. \quad (21)$$

Consequently, younger, rapidly rotating stars within a distance of 10 pc will be the most fruitful when observing thermal radio emission from stellar winds.

## 5 SUMMARY AND CONCLUSIONS

In this study, we presented wind simulations of eight solar analogues (including two of the Sun itself, from Carrington rotations 1983 and 2078) with a range of rotation rates and ages, using a fully 3D MHD code (Fig. 2). We selected a sample of solar-type stars and constrained the sample for which we had observations of their surface magnetic fields (Fig. 1). Other input parameters for our model include base temperatures and densities retrieved from semi-empirical laws scaled with rotation, equations (6)–(8) (Ó Fionnagáin & Vidotto 2018).

We demonstrated that the angular-momentum loss rate decreases steadily along with mass-loss rate over evolutionary time-scales (Fig. 3). Younger stars ($\approx 500$ Myr) rotating more rapidly ($P_{\mathrm{rot}} \approx 5$ d) display $\dot{J}$ values up to $\approx 10^{32}$ erg. The Sun (4.6 Gyr, $P_{\mathrm{rot}} = 27.2$ d) alternatively exhibits a much lower $\dot{J}$ at minimum $\approx 10^{30}$ erg, with significant variance of one order of magnitude over the solar magnetic cycle. The difference in solar $\dot{J}$ from minimum to maximum is explained by the greater amount of $\Phi_{\mathrm{open}}$ in the solar maximum case. Given that our solar maximum and minimum simulations differ, this incentivizes the monitoring of stars across entire magnetic cycles to deepen our understanding of stellar activity cycles (Jeffers et al. 2017, 2018). We found a similar declining rotation trend with $\dot{M}$ with slower rotators losing less mass than their faster rotating counterparts. Our solar analogues display a $\dot{M}$ ranging from $1 \times 10^{-13}$ to $5 \times 10^{-12}\,\mathrm{M}_\odot\,\mathrm{yr}^{-1}$.

We showed in Fig. 4 how the density, velocity, and ram pressures would vary for a hot Jupiter orbiting any of these solar-like stars at a distance of 0.1 au. We see that the sun at minimum provides the lowest ram pressures of the sample ($<10^5$ dyn cm$^{-2}$) while HD 190771 and $\chi^1$ Ori display the highest ram pressures with a maximum $>80 \times 10^{-5}$ dyn cm$^{-2}$. This is useful for any further studies on planetary environment within the winds of G-type stars, with the age and rotation of the host star indirectly playing a role in the final ram pressure impacting the planets and therefore upon atmospheric evaporation. We examined how the velocities of these stellar winds are distributed globally, by taking a histogram of velocities at a distance of 0.1 au, shown in Fig. 5. We showed that more magnetically active stars display less uniform density distributions and overall have a more complicated structure.

We developed a numerical tool for calculating thermal radio emission from stellar winds given a simulation grid, removing the need for analytical formulations that have been used in the past (Panagia & Felli 1975; Fichtinger et al. 2017; Vidotto & Donati 2017). This tool solves the radiative transfer equation for our wind models, which allowed us to derive radio flux densities, intensities, and spectra. We found emission around the μJy level with the winds staying optically thick up to 1–2 GHz. We compared our calculated flux densities with recent observations and found our predictions agree with the observational upper limits of $\kappa^1$ Ceti and $\chi^1$ Ori (Gaidos et al. 2000; F17). Previous radio detections have been interpreted as originating in the chromospheres of solar-like stars and not their winds (Villadsen et al. 2014; F17), which is supported by our simulations.

The normalized radio flux density emitted from these stellar winds is found to relate to stellar rotation as $S_{\nu,1\mathrm{GHz}} \propto \Omega^{0.9}$. This indicates that desired observational targets are stars with fast rotation rates within a distance of 10 pc. We showed in Fig. 8(a) that more active close by stars like $\chi^1$ Ori and $\kappa^1$ Ceti would be readily detectable with the next generation of radio telescopes such as SKA and ngVLA.

## ACKNOWLEDGEMENTS

The authors wish to acknowledge the DJEI/DES/SFI/HEA Irish Centre for High-End Computing (ICHEC) for the provision of computational facilities and support. This work used the BATS-R-US tools developed at the University of Michigan Center for Space Environment Modeling and made available through the NASA Community Coordinated Modeling Center. DÓF wishes to acknowledge funding received from the Trinity College Postgraduate Award through the School of Physics. AAV acknowledges funding received from the Irish Research Council Laureate Awards 2017/2018. SJ acknowledges the support of the German Science Foundation (DFG) Research Unit FOR2544 'Blue Planets around Red Stars', project JE 701/3-1 and DFG priority program SPP 1992 'Exploring the Diversity of Extrasolar Planets' (RE 1664/18). We thank Jackie Villadsen and Joe Llama for their useful discussion on topics of stellar radio emission. The authors would like to thank our referee, Dr Jorge Zuluaga, for his valuable input on this work.

*Software:* BATS-R-US (Powell et al. 1999), RADIOWINDS (Ó Fionnagáin 2018), SCIPY (Jones et al. 2001), MATPLOTLIB (Hunter 2007), and TECPLOT and SEABORN (Waskom et al. 2018).

## REFERENCES

Altschuler M. D., Newkirk G., 1969, Sol. Phys., 9, 131
Alvarado-Gómez J. D., Drake J. J., Cohen O., Moschou S. P., Garraffo C., 2018, ApJ, 862, 93
Anderson K. R., Storch N. I., Lai D., 2016, MNRAS, 456, 3671
Beck P. G. et al., 2017, A&A, 602, A63
Booth R. S., Poppenhaeger K., Watson C. A., Silva Aguirre V., Wolk S. J., Aguirre V. S., Wolk S. J., 2017, MNRAS, 471, 1012
Bower G. C., Loinard L., Dzib S., Galli P. A. B., Ortiz-León G. N., Moutou C., Donati J.-F., 2016, ApJ, 830, 107
Brown A. G. A., Vallenari A., Prusti T., de Bruijne J. H. J., Babusiaux C., Zurbach C., Zwitter T., 2018, A&A, 616, A1
Brown S. F., Donati J.-F., Rees D. E., Semel M., 1991, A&A, 250, 463
Brun A. S., Browning M. K., 2017, Living Rev. Sol. Phys., 14, 4
Cox A. N., Pilachowski C. A., 2002, Allen's Astrophysical Quantities, Vol. 53. Springer, New York
Cranmer S. R., Gibson S. E., Riley P., 2017, Space Sci. Rev., 212, 1345
Cranmer S. R., Saar S. H., 2011, ApJ, 741, 54
Crosley M. K. et al., 2016, ApJ, 830, 24
DeRosa M. L., Brun A. S., Hoeksema J. T., 2010, Proc. Int. Astron. Union, 6, 94
do Nascimento J.-D., Jr. et al., 2016, ApJ, 820, L15
Donati J.-F., Semel M., Carter B. D., Rees D. E., Cameron A. C., 1997, MNRAS, 291, 658
Fichtinger B., Güdel M., Mutel R. L., Hallinan G., Gaidos E., Skinner S. L., Lynch C., Gayley K. G., 2017, A&A, 599, A127 (F17)
Finley A. J., Matt S. P., See V., 2018, ApJ, 864, 125
Folsom C. P., Petit P., Bouvier J., Morin J., Lèbre A., Donati J.-F., 2016, MNRAS, 10, 113
Folsom C. P. et al., 2018, MNRAS, 474, 4956
Gaidos E. J., Güdel M., Blake G. A., 2000, Geophys. Res. Lett., 27, 501
Gallet F., Bouvier J., 2013, A&A, 556, A36
Gallet F., Bouvier J., 2015, A&A, 577, A98
Güdel M., 2002, ARA&A, 40, 217

Güdel M., 2007, Living Rev. Sol. Phys., 4, 3
Güdel M., Guinan E. F., Skinner S., 1998, PASP, 154, 1041
Holzwarth V., Jardine M., 2007, A&A, 463, 11
Huber D. et al., 2013, Science, 342, 331
Hunter J. D., 2007, Comput. Sci. Eng., 9, 90
Jeffers S. V., Saikia S. B., Barnes J. R., Petit P., Marsden S. C., Jardine M. M., Vidotto A. A., 2017, MNRAS, 471, L96
Jeffers S. V. et al., 2018, MNRAS, 479, 5266
Johnstone C. P., Güdel M., Brott I., Lüftinger T., 2015b, A&A, 577, A28
Johnstone C. P., Güdel M., Lüftinger T., Toth G., Brott I., 2015a, A&A, 577, A27
Jones E. et al., 2001,, SciPy: Open Source Scientific Tools for Python, http://www.scipy.org/
Lang P., Jardine M., Morin J., Donati J.-F., Jeffers S., Vidotto A. A., Fares R., 2014, MNRAS, 439, 2122
Lehmann L. T., Jardine M. M., Mackay D. H., Vidotto A. A., 2018, MNRAS, 478, 4390
Lim J., White S. M., 1996, ApJ, 462, L91
Lorenzo-Oliveira D. et al., 2018, A&A, 619, A73
Maehara H., Notsu Y., Notsu S., Namekata K., Honda S., Ishii T. T., Nogami D., Shibata K., 2017, PASJ, 69
Maldonado J., Martínez-Arnáiz R. M., Eiroa C., Montes D., Montesinos B., 2010, A&A, 521, A12
Manchester W. et al., 2008, ApJ, 684, 1448
Matt S. P. S., MacGregor K. K. B., Pinsonneault M. M. H., Greene T. P. T., 2012, ApJ, 754, L26
Meléndez J. et al., 2014, ApJ, 791, 14
Messina S., Guinan E. F., 2003, A&A, 409, 1017
Mestel L., 1999, Stellar Magnetism. Oxford Univ. Press, Oxford
Metcalfe T. S., Egeland R., van Saders J., 2016, ApJ, 826, L2
Nicholson B. A. et al., 2016, MNRAS, 459, 1907
Noyes R. W., Hartmann L. W., Baliunas S. L., Duncan D. K., Vaughan A. H., 1984, ApJ, 279, 763
Osten R. A., , Crosley M. K., Gudel M., Kowalski A. F., Lazio J., Linsky J., Murphy E., White S., 2018, preprint (arXiv:1803.05345)
Ó Fionnagáin D., Vidotto A. A., 2018, MNRAS, 476, 2465
Ó Fionnagáin D. (Version v0.0.5), Zenodo, 2018, ofionnad/radiowinds: Calculating Thermal Bremsstrahlung Emission from Stellar Wind
Owen J. E., Mohanty S., 2016, MNRAS, 459, 4088
Panagia N., Felli M., 1975, A&A, 39, 1
Pantolmos G., Matt S. P., 2017, ApJ, 849, 83
Petit P., Dintrans B., Morgenthaler A., Van Grootel V., Morin J., Lanoux J., Aurière M., Konstantinova-Antova R., 2009, A&A, 508, L9
Petit P. et al., 2008, MNRAS, 388, 80
Pognan, Q., Garraffo, C., Cohen, O., Drake, J., 2018, ApJ, 856, 53
Pope B. J. S., Withers P., Callingham J. R., Vogt M. F., 2018, preprint (arXiv:1810.11493)
Powell K. G., Roe P. L., Linde T. J., Gombosi T. I., De Zeeuw D. L., 1999, J. Comp. Phys., 154, 284
Prusti T. et al., 2016, A&A, 595, A1
Reynolds S. P., 1986, ApJ, 304, 713
Ribas I. et al., 2016, A&A, 596, A111
Rosén L., Kochukhov O., Hackman T., Lehtinen J., 2016, A&A, 593, A35
Rucinski S. M. et al., 2004, PASP, 116, 1093
Réville V., Brun A. S., Matt S. P., Strugarek A., Pinto R. F., 2015, ApJ, 798
Réville V., Folsom C. P., Strugarek A., Brun A. S., 2016, ApJ, 832, 145
See V., Jardine M., Vidotto A. A., Petit P., Marsden S. C., Jeffers S. V., do Nascimento J. D., 2014, A&A, 570, A99
See V. et al., 2017a, MNRAS , 466, 1542
See V. et al., 2017b, MNRAS, 466, 1542
Semel M., 1989, A&A, 225, 456
Skumanich A., 1972, ApJ, 171, 565
Solanki S. K., Inhester B., Schüssler M., 2006, Rep. Prog. Phys., 69, 563
Suzuki T. K., Imada S., Kataoka R., Kato Y., Matsumoto T., Miyahara H., Tsuneta S., 2013, PASJ, 65, 98
Telleschi A., Gudel M., Briggs K., Audard M., Ness J., Skinner S. L., 2005, ApJ, 622, 653
Tóth G. et al., 2005, J. Geophys. Res., 110, A12226
Valenti J. A., Fischer D. A., 2005, A&AS, 159, 141
Van Doorsselaere T., Wardle N., Zanna G. D., Jansari K., Verwichte E., Nakariakov V. M., 2011, ApJ, 727, L32
Van Saders J. L., Ceillier T., Metcalfe T. S., Aguirre V. S., Pinsonneault M. H., García R. A., Mathur S., Davies G. R., 2016, Nature, 529, 181
Verdini A., Velli M., Matthaeus W. H., Oughton S., Dmitruk P., 2010, ApJ, 708, L116
Vidotto A., 2017, EPJ Web Conf., 160, 05011
Vidotto A. A., 2016, MNRAS, 459, 1533
Vidotto A. A., Donati J.-F., 2017, A&A, 602, A39
Vidotto A. A., Fares R., Jardine M., Moutou C., Donati J.-F. F., 2015, MNRAS, 449, 4117
Vidotto A. A., Jardine M., Morin J., Donati J. F., Opher M., Gombosi T. I., 2014a, MNRAS, 438, 1162
Vidotto A. A., Lehmann L., Jardine M., Pevtsov A., 2018, MNRAS, 12, 1
Vidotto A. A. et al., 2014b, MNRAS, 441, 2361
Villadsen J., Hallinan G., Bourke S., Güdel M., Rupen M., 2014, ApJ, 788, 112
Waskom M. et al., 2018,mwaskom/seaborn: v0.9.0 (July 2018),
Weber E. J. E. E. J., Davis, Leverett J., Davis L., Jr., Davis, Leverett J., 1967, ApJ, 148, 217
Wood B. E., Müller H.-R., Zank G. P., Linsky J. L., Redfield S., 2005, ApJ, 628, L143
Wright A. E., Barlow M. J., Michael J., 1975, MNRAS, 170, 41
Wright N. J., Drake J. J., Mamajek E. E., Henry G. W., 2011, ApJ, 743, 48

## APPENDIX A: EFFECTS OF DENSITY AND ITS GRADIENT ON RADIO EMISSION

Many previous analytical works have shown the strong dependence of thermal free–free radio emission on density gradients in the wind (Panagia & Felli 1975; Wright et al. 1975; Lim & White 1996). We show in Fig. A1 how the flux density spectrum for $\kappa^1$ Ceti would change given a density gradient that follows $n \propto R^{-2}$ (green line), and in addition one that has a constant temperature (red line). Both of these models have a base density three times less than the original spectrum (blue line). We see that this slower density decay has a dramatic affect on the shape of the spectrum in the optically thick regime. The density gradient for our simulation varies across the grid, but in nearly all cases it is much steeper than $n \propto R^{-2}$. The

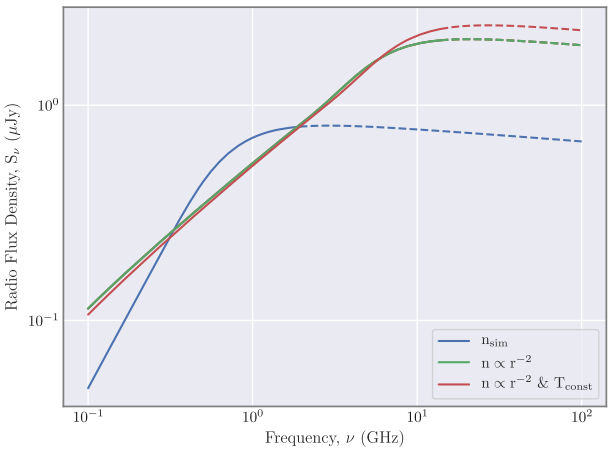


**Figure A1.** The blue line shows the same spectrum for $\kappa^1$ Ceti as shown in Fig. 8(a). The green line represents the same grid, with the same temperature gradient, but with a density that falls off with $R^{-2}$. The base density for this green line is also a factor of 3 smaller than the blue line. The red line represents the same scenario as the green line but with a constant temperature across the grid. Here we can see the huge impact density gradient has on flux density and spectrum shape.

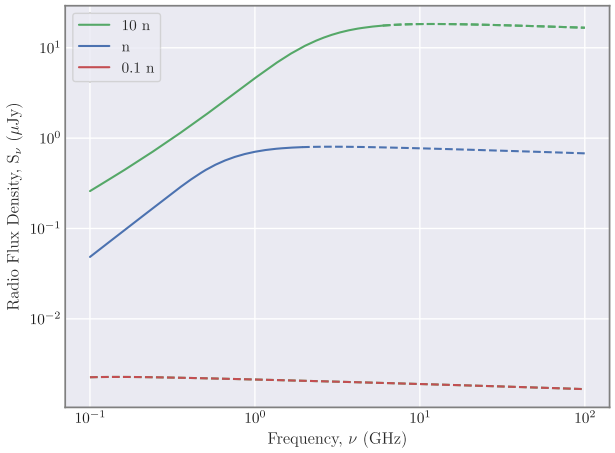


**Figure A2.** The blue line shows the same spectrum for $\kappa^1$ Ceti as shown in Fig. 8(a). The green line represents the same density structure with 10 times the original density, and the red line represents the original density divided by a factor of 10. The dashed portion of each line represents where the wind becomes optically thin. We see in the low-density case that the entire wind is optically thin and emission is very low as there is an extremely tenuous wind. For the high-density case we see much higher fluxes, and the wind is optically thick for most of the observing frequencies in our range.

steeper decay of density causes the emission to be lower across all frequencies. The temperature gradient has a minimal effect on spectrum shape compared to the density.

Fig. A2 shows how the density of the wind will affect the overall emission, changing where the wind becomes optically thick/thin, and the increase/decrease in the flux density. This is relevant to observations because, if two or more detections are made at different frequencies and follow the optically thin power law of $\propto \nu^{-0.1}$, then we can assume the wind is thin and therefore constrain the value for density in the wind. In the low-density case the entire wind is optically thin and emission is very low as there is an extremely tenuous wind. For the high-density case we see much higher fluxes, and the wind is optically thick for most of the observing frequencies in our range.

This paper has been typeset from a TEX/LATEX file prepared by the author.